Optics Letters

Tunable dual-band asymmetric transmission for circularly polarized waves with graphene planar chiral metasurfaces

Zhancheng Li,[1] Wenwei Liu,[1] Hua Cheng,[1] Shuqi Chen,[1,*] and Jianguo Tian[1,2]

[1]The Key Laboratory of Weak Light Nonlinear Photonics, Ministry of Education, School of Physics and Teda Applied Physics Institute, Nankai University, Tianjin 300071, China
[2]e-mail: jjtian@nankai.edu.cn
*Corresponding author: schen@nankai.edu.cn

Received 12 May 2016; revised 9 June 2016; accepted 11 June 2016; posted 13 June 2016 (Doc. ID 265090); published 1 July 2016

The asymmetric transmission effect has attracted great interest due to its wide modern optical applications. In this Letter, we present the underlying theory, the design specifications, and the simulated demonstration of tunable dual-band asymmetric transmission for circularly polarized waves with a graphene planar chiral metasurface. The spectral position of the asymmetric peak is linearly dependent on the Fermi energy and can be controlled by changing the Fermi energy. The success of tunable dual-band asymmetric transmission can be attributed to the enantiomerically sensitive plasmonic excitations of the graphene metasurface. This work offers a further step in developing tunable asymmetric transmission of circularly polarized waves for applications in detectors and other polarization-sensitive electromagnetic devices.

OCIS codes: (160.3918) Metamaterials; (240.6680) Surface plasmons; (120.7000) Transmission.

http://dx.doi.org/10.1364/OL.41.003142

Chirality in metasurfaces has attracted a great deal of attention both for theoretical research and practical applications, since it is exceedingly useful in constructing electromagnetic devices [1–4]. Asymmetric transmission in planar chiral structure, which manifests itself as a difference in the total transmission between forward and backward propagations, has been an active field of research for quite some time since its first experimental demonstration [5]. Based on the concept of asymmetric transmission, electromagnetic devices such as polarization transformers and polarization-controlled devices have been proposed for both linearly and circularly polarized waves, which have a myriad applications in spectroscopy, ultrafast information processing, optical interconnects, communications, and so on [6–15]. The realization of asymmetric transmission for circularly polarized waves in planar chiral metasurfaces always associates with the excitation of enantiomerically sensitive plasmons in metasurface nanostructures [2,6]. Controlling this plasmon excitation of metasurfaces actively will enable dynamic tunability of the asymmetric transmission and potentially expand the range of asymmetric transmission applications even further. However, the tunability of the plasmon excitation in metasurfaces has to be controlled by accurately fabricating different nanostructures in the previous works, which is an inherent drawback [14,16,17]. Moreover, the proposed asymmetric transmission devices always have complex structures which prevent its real applications in modern optical systems.

Graphene is a monolayer of hexagonally arranged carbon atoms, can support the excitation of surface plasmons in the mid-infrared regime, and its optical response shows a strong dependence on the Fermi energy, which can be dynamically controlled by a gate voltage [18,19]. Therefore, graphene is a promising electrically tunable plasmonic material. The investigation of tunable plasmons in graphene nanostructures has led to the proposition and demonstration of a variety of applications such as tunable polarization conversion [20–22], tunable plasmonically induced transparency [23,24], tunable anomalous refraction [25] and tunable perfect absorption [26,27].

In this Letter, we present the underlying theory, the design specifications, and the simulated demonstration of a tunable dual-band asymmetric transmission for circularly polarized waves in the mid-infrared regime by a graphene planar chiral metasurface. This asymmetric transmission can dynamically shift with the change of the graphene's Fermi energy. The simulated results further verify the design predictions and agree well with the theoretical analysis. Moreover, we demonstrate that the asymmetric peak is sensitive and almost linearly related with changing the graphene's Fermi energy while keeping the performance of the asymmetric transmission.

The realization of the asymmetric transmission for circularly polarized waves can be well presented in theory by using Jones matrices descriptions of the optical system. The transmission of coherent light through any dispersive optical system can be described by means of complex Jones matrices **T** [28]. Accordingly, the transmittances in the two opposite propagation directions for left-handed polarization can be expressed with **T**-matrix elements as

$$T^{\mathrm{f}} = |t_{\mathrm{LL}}|^2 + |t_{\mathrm{RL}}|^2, \tag{1a}$$

$$T^{b} = |t_{LL}|^2 + |t_{LR}|^2. \quad \textbf{(1b)}$$

Then, the asymmetric transmission can be defined as the difference between the transmitted intensities for different propagation directions. For the circular base, it can be expressed as

$$\Delta T = \Delta_{circ}^{LCP} = |t_{RL}|^2 - |t_{LR}|^2 = -\Delta_{circ}^{RCP}. \quad \textbf{(2)}$$

Obviously, the effect of asymmetric transmission for circular polarization is entirely determined by the magnitude difference between the **T**-matrix elements t_{RL} and t_{LR} of the system.

The proposed graphene metasurface is constructed with a 2D chiral pattern because the magnitude difference of t_{RL} and t_{LR} can be easily realized with enantiomerically sensitive plasmonic excitations in the planar chiral structures. Figure 1(a) illustrates the artistic rendering of the proposed asymmetric transmission of the graphene planar chiral metasurface, where the transmission intensity along the $+z$ (forward) and $-z$ (backward) directions with any circularly polarized incident wave are different in the working bandwidth. The working bandwidth can be dynamically controlled with the change of the graphene's Fermi energy by varying the gate voltage of the parallel capacitor. The structure parameters of the graphene metasurface are shown in Fig. 1(b), where the graphene sheet covers the entire substrate. The proposed structure is based on a cut-out design of split rings in orthogonal orientation, forming a two-dimensionally chiral pattern, which is a Babinet structure in Ref. [6]. It could realize asymmetric transmission for circular polarization predicated by theory. The geometric parameters are not complicated, and the cut-out design is responsible for gate voltage in its real applications. The purpose of choosing this design is to provide a concise and effective comparison on efficiency and the underlying physics of asymmetric transmission between graphene and metallic metasurfaces.

Numerical simulations have been conducted to analyze the characterizations of the proposed graphene metasurface, which were carried out by using CST microwave studio [29]. In our simulations, periodic boundary conditions were set in x and y directions, representing a periodical structure, and an open (perfectly matching layer) boundary was defined in the z direction for light incidence and transmission, while the excitation source was either a left- or right-handed circularly polarized plane wave. The mesh size of the graphene was generated by using the self-adaption method to ensure that the mesh size is small enough for an accurate simulation result. The permittivity of the substrate is taken as 2.25. The thickness of the graphene layer is set as $t = 1$ nm. The graphene layer is regarded as an anisotropic material with in-plane conductivity $\sigma_{\parallel}$ and out-of-plane permittivity $\varepsilon_{\perp}$. This method mainly focuses on the material effect in 2D flat surface while ignoring that in the out-of-plane direction, which can simulate a 2D current in the graphene layer under the local electric field. The out-of-plane dielectric constant of graphene remains at 2.25, which is the permittivity of the substrate material and has tiny effects in the simulation results due to the thinness of graphene. When the light frequency is smaller than the optical phonon frequency, both interband damping and plasmon decay via excitation of an optical phonon together with an electron–hole pair are inactive. In this case, the intrinsic relaxation time can be estimated from DC mobility and can be expressed as $\tau = \mu E_F / e v_F^2$ [30], where $v_F \approx c/300$ is the Fermi velocity, and $\mu = 10,000\ \mathrm{cm^2/Vs}$ is the DC mobility [31]. The in-plane conductivity of graphene is calculated within the local random phase approximation at temperature $T = 300$ K [23].

To make a comparison with the theoretical analysis, we calculated four transmission matrix elements **T** of the proposed graphene chiral planar metasurface. Figures 2(a) and 2(b) show the calculated results of the squared moduli $T_{ij} = |t_{ij}|^2$ for forward and backward propagation at the Fermi energy $E_F = 0.9$ eV, respectively. As shown by red solid line and green dotted line, respectively, T_{LL} and T_{RR} are identical and independent of the handedness of the incident circularly polarized wave. T_{LL} and T_{RR} are also reciprocal and independent of the direction of propagation. This means that the proposed graphene metasurface does not show any significant circular dichroism over the whole presented spectral range. In contrast to the direct transmissions T_{LL} and T_{RR}, the conversional transmissions T_{RL} and T_{LR} depend on both the direction of propagation and the handedness of the incident circularly polarized wave. According to Eq. (2), the magnitude difference between the conversional transmissions T_{RL} and T_{LR} indicates

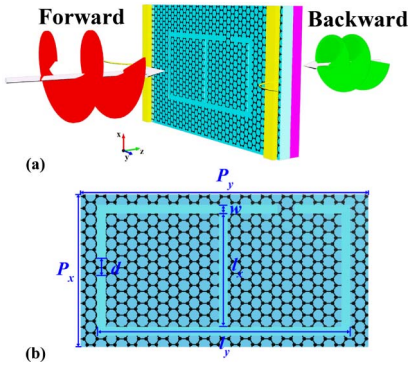

Fig. 1. (a) An artistic rendering of the asymmetric transmission in the graphene planar chiral metasurface. (b) A unit cell with structure parameters. The period in x and y directions are $P_x = 250$ nm and $P_y = 300$ nm, respectively. The length of the short and long hollow are $l_x = 80$ nm and $l_y = 240$ nm, respectively. The width of all the hollows is $w = 20$ nm. The length of the gaps is $d = 30$ nm.

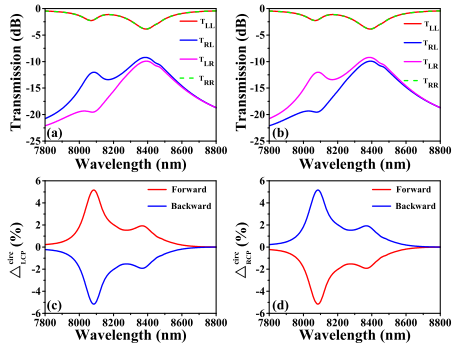

Fig. 2. Calculated squared moduli $T_{ij} = |t_{ij}|^2$ of the graphene planar chiral metasurface for (a) forward propagation and (b) backward propagation. Asymmetric transmission for (c) left-handed and (d) right-handed circularly polarized waves propagating along either forward or backward direction. The Fermi energy is fixed at 0.90 eV.

the presence of asymmetric transmission. The asymmetric transmissions of the proposed graphene metasurface are shown in Figs. 2(c) and 2(d), where the Fermi energy is fixed at $E_F = 0.9$ eV. Two asymmetric transmission peaks with the values of 5.2% and 1.9% at the wavelengths of 8085 nm and 8370 nm, respectively, can be obviously observed. The asymmetric transmission efficiency of our proposed graphene metasurface is consistent with that of the previous metallic metamaterials, while the size of the graphene metasurface is tens of times less [6]. Moreover, the asymmetric transmission exists in the wavelength range of 7800–8600 nm, and the value of asymmetric transmission is opposite for forward and backward directions, following Eq. (2).

The asymmetric transmission of the proposed metasurface is attributed to the enantiomerically sensitive plasmons inducing the charge-field excitations. To show the underlying physics of the asymmetric transmission peaks, we show the resonance-induced current density magnitude and the local electric distribution in the cut-out area of the metasurface in Fig. 3. The electric field distribution without the graphene metasurface is also shown in the inset of Fig. 3(a). The strong asymmetric transmission peak at 8085 nm is attributed to the significantly spin-dependent polarization conversion, as shown in Figs. 3(a) and 3(b). T_{RL} and T_{LR} for left circular polarization (LCP) and right circular polarization (RCP) incidences are decided by the induced electric field components in x direction, as indicated by the red and blue arrows. The direction of the blue arrows is opposite to that of the red arrows, which suppresses the conversional transmissions. Moreover, the magnitude of the blue arrows for the RCP incidence is larger than that for the LCP incidence, which produces a significant asymmetric transmission as T_{LR} is smaller than T_{RL}. For the weak peak at 8370 nm, the induced electric field components in x direction indicated by red arrows in Figs. 3(c) and 3(d) are more powerful compared with those in Figs. 3(a) and 3(b), and they have no opposite components. Thus, T_{RL} and T_{LR} at 8370 nm are larger than those at 8085 nm. The weak asymmetric transmission at 8370 nm is mainly attributed to the difference between T_{RL} and T_{LR}, which is caused by the difference of the induced intensity, as indicated by blue dashed squares.

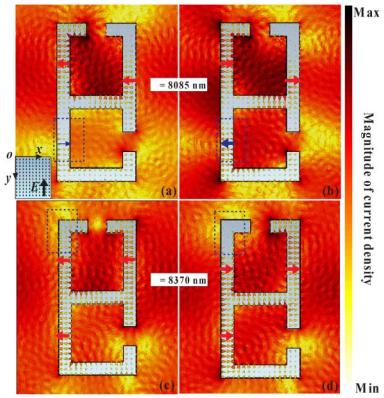

Fig. 3. Maps of the magnitude of the resonance-induced current density and the local electric distribution in the hole area of the metasurface (a),(c) left-handed polarized and (b),(d) right-handed polarized waves propagating along the forward direction at the wavelengths of 8085 nm and 8370 nm, respectively. The Fermi energy is fixed at 0.90 eV. Inset of (a): the electric field distribution without the graphene metasurface.

To show the tunability of the asymmetric transmission, we analyzed the influence of the graphene's Fermi energy E_F on the transmission matrix elements and the value of the asymmetric transmission in Fig. 4. The squared moduli $T_{ij} = |t_{ij}|^2$ for forward propagations at different Fermi energies are shown in Figs. 4(a)–4(c). With decreasing Fermi energy E_F, the curves of the direct transmissions (T_{LL} and T_{RR}) and the conversional transmissions (T_{RL} and T_{LR}) move toward longer wavelengths, while the shapes of the curves do not change. Meanwhile, the values of asymmetric transmissions for forward propagations at different Fermi energies are shown in Figs. 4(d)–4(f). The variation of the asymmetric transmission value is consistent with four transmission matrix elements. Obviously, by changing Fermi energy, the asymmetric transmission can be realized in a wide bandwidth while maintaining the performance of the asymmetric transmission.

To investigate the relationship between the asymmetric transmission and the graphene's Fermi energy, we calculated the dynamic tunability of the asymmetric transmission for forward propagation in Fig. 5(a). The blue and green lines indicate the shift of asymmetric transmission peaks. Both the strong and weak asymmetric transmission peaks have a redshift with decreasing Fermi energy, and the wavelength shift is almost linearly related with the Fermi energy. The linear dependence of the resonance wavelength on the Fermi energy is attributed to the relation between the optical response and the Fermi energy of the graphene. The real part of the graphene's permittivity has a linear relationship with changing Fermi energy, while its imaginary part almost keeps constant in a large wavelength range, as shown in Figs. 5(b) and 5(c). Moreover, both the strong and weak asymmetric transmission peaks will shift about 750 nm when the Fermi energy is changed by 0.16 eV. Thus, the dynamic and sensitive tunability of the asymmetric transmission based on the graphene planar chiral metasurface will potentially expand the range of its applications even further. The DC mobility μ in the single layer graphene usually varies in the range from $\mu = 3000$ cm^2/Vs to $\mu = 10,000$ cm^2/Vs [31]. Therefore, the intrinsic relaxation time will vary in the range from 0.27 to 0.90 ps when the Fermi energy is fixed at 0.9 eV. To further discuss the dependence of the amplitude of the asymmetric transmission on the intrinsic relaxation time, we give the asymmetric transmission spectra for different

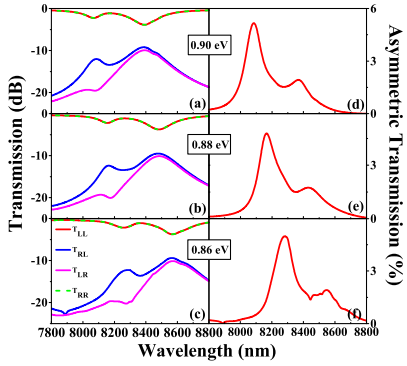

Fig. 4. (a)–(c) The squared moduli $T_{ij} = |t_{ij}|^2$ of four transmission matrix elements, and (d)–(f) the asymmetric transmission for forward propagation at different Fermi energies.

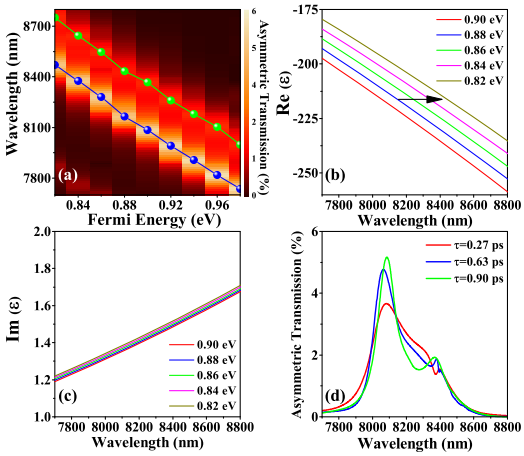

Fig. 5. (a) Asymmetric transmission as a function of wavelength and Fermi energy for forward propagation. Green and blue lines indicate the shift of the strong and weak asymmetric transmission peaks, respectively. (b) The real part and (c) the imaginary part of the graphene's permittivity as a function of the Fermi energy. (d) Asymmetric transmission spectra for different intrinsic relaxation times, where the Fermi energy is fixed at 0.9 eV.

intrinsic relaxation times in Fig. 5(d). With the decrease of intrinsic relaxation time, the peak amplitude of the asymmetric transmission will gradually decrease.

In summary, we proposed a simulated investigation and theoretical analysis of a tunable dual-band asymmetric transmission for circularly polarized incident waves in the mid-infrared regime. Theoretical analysis shows that the asymmetric transmission for circular polarization can be obtained by the realization of the difference between the conversional transmission coefficients. To verify the theoretical predictions, a graphene planar chiral metasurface, which is based on a cut-out design of split rings in orthogonal orientation, is designed and investigated. The simulated results confirmed the tunable dual-band asymmetric transmission for circularly polarized waves along opposite propagation directions. In particular, the physical mechanism of this graphene metasurface is based on the enantiomerically sensitive plasmonic excitations of the 2D planar chiral pattern, and the asymmetric transmission peaks are sensitive to the graphene's Fermi energy. This result offers helpful insight and provides intriguing possibilities for the design of devices based on sensitive tunable asymmetric transmission of circular polarization.

Funding. National Basic Research Program (973 Program) of China (2012CB921900); National Natural Science Foundation of China (NSFC) (1130416311574163, 61378006); Program for New Century Excellent Talents in University (NCET-13-0294); 111 Project (B07013).

REFERENCES

1. E. Plum, V. A. Fedotov, and N. I. Zheludev, Appl. Phys. Lett. **93**, 191911 (2008).
2. E. Plum, V. A. Fedotov, and N. I. Zheludev, Appl. Phys. Lett. **94**, 131901 (2009).
3. S. Yang, W. Chen, R. L. Nelson, and Q. Zhan, Opt. Lett. **34**, 3047 (2009).
4. Y. Zhao, M. A. Belkin, and A. Alú, Nat. Commun. **3**, 870 (2012).
5. V. A. Fedotov, P. L. Mladyonov, S. L. Prosvirnin, A. V. Rogacheva, Y. Chen, and N. I. Zheludev, Phys. Rev. Lett. **97**, 167401 (2006).
6. R. Singh, E. Plum, C. Menzel, C. Rockstuhl, A. K. Azad, R. A. Cheville, F. Lederer, W. Zhang, and N. I. Zheludev, Phys. Rev. B **80**, 153104 (2009).
7. Z. Wei, Y. Cao, Y. Fan, X. Yu, and H. Li, Appl. Phys. Lett. **99**, 221907 (2011).
8. J. Han, H. Li, Y. Fan, Z. Wei, C. Wu, Y. Cao, X. Yu, F. Li, and Z. Wang, Appl. Phys. Lett. **98**, 151908 (2011).
9. M. Mutlu, A. E. Akosman, A. E. Serebryannikov, and E. Ozbay, Phys. Rev. Lett. **108**, 213905 (2012).
10. J. Shi, X. Liu, S. Yu, T. Lv, Z. Zhu, H. F. Ma, and T. J. Cui, Appl. Phys. Lett. **102**, 191905 (2013).
11. Z. Li, S. Chen, C. Tang, W. Liu, H. Cheng, Z. Liu, J. Li, P. Yu, B. Xie, Z. Liu, J. Li, and J. Tian, Appl. Phys. Lett. **105**, 201103 (2014).
12. L. Wu, Z. Yang, Y. Cheng, M. Zhao, R. Gong, Y. Zheng, J. Duan, and X. Yuan, Appl. Phys. Lett. **103**, 021903 (2013).
13. Z. Li, M. Mutlu, and E. Ozbay, J. Phys. D **47**, 075107 (2014).
14. J. H. Shi, H. F. Ma, C. Y. Guan, Z. P. Wang, and T. J. Cui, Phys. Rev. B **89**, 165128 (2014).
15. Z. Li, S. Chen, W. Liu, H. Cheng, Z. Liu, J. Li, P. Yu, B. Xie, and J. Tian, Plasmonics **10**, 1703 (2015).
16. D. Liu, Z. Xiao, X. Ma, L. Wang, K. Xu, J. Tang, and Z. Wang, Appl. Phys. A **118**, 787 (2015).
17. Y. Xu, Q. Shi, Z. Zhu, and J. Shi, Opt. Express **22**, 25679 (2014).
18. F. H. L. Koppens, D. E. Chang, and F. J. García de Abajo, Nano Lett. **11**, 3370 (2011).
19. J. Chen, M. Badioli, P. Alonso-Gonzàlez, S. Thongrattanasiri, F. Huth, J. Osmond, M. Spasenović, A. Centeno, A. Pesquera, P. Godignon, A. Z. Elorza, N. Camara, F. J. García de Abajo, R. Hillenbrand, and F. H. L. Koppens, Nature **487**, 77 (2012).
20. H. Cheng, S. Chen, P. Yu, J. Li, B. Xie, Z. Li, and J. Tian, Appl. Phys. Lett. **103**, 223102 (2013).
21. J. Li, P. Yu, H. Cheng, W. Liu, Z. Li, B. Xie, S. Chen, and J. Tian, Adv. Opt. Mater. **4**, 91 (2016).
22. H. Cheng, S. Chen, P. Yu, J. Li, L. Deng, and J. Tian, Opt. Lett. **38**, 1567 (2013).
23. J. Ding, B. Arigong, H. Ren, M. Zhou, J. Shao, M. Lu, Y. Chai, Y. Lin, and H. Zhang, Sci. Rep. **4**, 6128 (2014).
24. H. Cheng, S. Chen, P. Yu, X. Duan, B. Xie, and J. Tian, Appl. Phys. Lett. **103**, 203112 (2013).
25. H. Cheng, S. Chen, P. Yu, W. Liu, Z. Li, J. Li, B. Xie, and J. Tian, Adv. Opt. Mater. **3**, 1744 (2015).
26. S. Thongrattanasiri, F. H. L. Koppens, and F. J. García de Abajo, Phys. Rev. Lett. **108**, 047401 (2012).
27. Y. Fan, N.-H. Shen, T. Koschny, and C. M. Soukoulis, ACS Photon. **2**, 151 (2015).
28. C. Menzel, C. Helgert, C. Rockstuhl, E.-B. Kley, A. Tünnermann, T. Pertsch, and F. Lederer, Phys. Rev. Lett. **104**, 253902 (2010).
29. CST Studio Suite, Version (Computer Simulation Technology AG, 2015), www.cst.com.
30. M. Jablan, H. Buljan, and M. Soljačić, Phys. Rev. B **80**, 245435 (2009).
31. K. S. Novoselov, A. K. Geim, S. V. Morozov, D. Jiang, Y. Zhang, S. V. Dubonos, I. V. Grigorieva, and A. A. Firsov, Science **306**, 666 (2004).